Combustion and Flame 225 (2021) 513–523

Contents lists available at ScienceDirect

Combustion and Flame

journal homepage: www.elsevier.com/locate/combustflame

Thermoacoustic instability analysis of a laminar lean premixed flame under autoignitive conditions

Zongming Yu[a,b,c,*], Yuhua Ai[a,b,c], Yue Wang[a,b,c,d], Chuanzhi Luo[a,b,c,d]

[a] Innovation Academy for Light-duty Gas Turbine, Chinese Academy of Sciences, Beijing 100190, China
[b] Key Laboratory of Advanced Energy and Power, Institute of Engineering Thermophysics, Chinese Academy of Sciences, Beijing 100190, China
[c] Advanced Gas Turbine Laboratory, Institute of Engineering Thermophysics, Chinese Academy of Sciences, Beijing 100190, China
[d] University of Chinese Academy of Sciences, Beijing 100049, China

ARTICLE INFO

Article history:
Received 4 August 2020
Revised 19 November 2020
Accepted 19 November 2020

Keywords:
Lean premixed flame
Autoignition
Laminar flame propagation
Thermoacoustic instability
Diesel fuel

ABSTRACT

To address engineering challenges encountered in developing advanced gas turbine combustors, theoretical analysis and numerical simulation were performed to investigate the thermoacoustic instability of a laminar lean premixed flame under autoignitive conditions. The analysis was carried out within the scope of weak autoignition tendencies and employed a three-step mechanism, which included the chain-initiation reaction. The numerical simulation was performed as a validation using a skeletal mechanism for diesel fuel under the typical operating conditions of gas turbines. The results showed that the three-step mechanism could qualitatively describe the high-temperature chemistry involved in autoignition and flame propagation. The analysis indicated that the flame propagation speed was accelerated by the accumulation of pre-flame reactions. Under certain conditions, the flame speed showed a linear correlation with the pre-flame length. The results were consistent with the existing literature. In addition, the equilibrium position of the flame oscillation, which was excited by velocity fluctuation, could return to the initial position, and pre-flame reactions could alter the phase delay. These results suggested a new mechanism for thermoacoustic instability because the overall heat release rate fluctuated with the flame front. The flame might amplify, damp, high-pass filter, or low-pass filter the acoustic energy based on the phase difference between the velocity and pressure oscillations.

1. Introduction

Lean premixed combustion has been widely adopted in modern gas turbine engines to reduce pollutant emissions [1]. As engine efficiency is continuously improving, pressure and temperature at the combustor inlet increase accordingly, which leads to a reduction of the autoignition delay time of fuel-air mixtures. For typical cases, this time scale is reduced to 1–10 ms [2,3], becoming one of the most important constraints in fuel-air mixing design [4]. This time scale is exploited in engineering to achieve a desired mixing uniformity for low-emission combustion. However, because the reactant mixture is autoignitive, which deviates from the classical models, another issue emerges regarding the process of flame propagation and its aerodynamic characteristics [5]. "Autoignitive" has been defined as a condition where the flow residence time (τ_f) is comparable to the autoignition delay time (τ_{ig}), and the flame propagation process is notably coupled to the chemical process of autoignition [6–18]. The engineering needs for improving prediction models and design methods have been driving academic investigations on combustion behavior under such conditions.

Won et al. [6,7] and Windom et al. [8,9] conducted experimental studies to measure the turbulent premixed flame speed at varying flow residence times with a reactor assisted turbulent slot burner. They observed a strong CH_2O signal in the unburned regime upstream of the flame front, which indicated that pre-flame reactions occur at elevated temperatures. Their results also indicated that the turbulent flame might be drastically accelerated by the pre-flame reactions changing the reactant composition and Lewis number. They observed a potential flame instability mode caused by a leap in the flame speed due to pre-flame reactions. Krisman et al. [10] performed a comprehensive numerical investigation on laminar premixed flames under autoignitive conditions. Their results showed that both single-stage and two-stage ignition fuels could form an autoignition-assisted flame, which propagated mainly owing to a diffusion-reaction balance as the flow residence time was comparable to the ignition delay time. Consistent

* Corresponding author at: No. 11, North-western Section of 4th Ring, Beijing 100190, China.
E-mail address: yuzongming@iet.cn (Z. Yu).

https://doi.org/10.1016/j.combustflame.2020.11.032
0010-2180/

with experimental results, their results showed that pre-flame reactions could significantly modify the reactant stream ahead of the reaction zone and thus assist flame propagation. The results of further numerical studies [11–14] showed that the profile of normalized flame speed might have a “hockey-stick” shape, which suggested a strong nonlinearity lay in the transition from flame propagation to autoignition.

Schulz et al. [15–17] and Ebi et al. [18] performed a series of numerical and experimental studies on the aerodynamics of methane flames in sequential combustors. Their results showed that autoignition and flame propagation could co-exist in a turbulent reacting flow. Furthermore, the transition of burning modes could trigger a sudden change in the local heat release rate, driving the flame to oscillate with high amplitude. It was essential to suppress such phenomenon in engineering. However, classical thermoacoustic models [19] could not describe its mechanism since the flame speed was no longer constant through the spatial location or flow residence time.

This work aimed at understanding the impact of pre-flame reactions on thermoacoustic instability within the scope of a laminar lean premixed flame under the operating conditions of an advanced industrial gas turbine. The remainder of this paper is organized as follows. Section 2 presents a semi-infinite one-dimensional model used for the theoretical analysis of the flame structure, its propagation, and its response to flow oscillation under autoignitive conditions. Section 3 presents a detailed numerical simulation performed with surrogate diesel fuel under inlet conditions of 3 MPa and 860 K. The results were used to examine the chemical structure of the premixed flame and the validity of the previous analysis. Section 4 concludes the study presented in this paper.

2. Theoretical analysis

2.1. Chemical reactions

To fully describe the chemistry of flame propagation and fuel autoignition, a three-step mechanism [5,20] was employed for the theoretical analysis:

$$F + M \rightarrow R + M \qquad r_I = A_I \rho^2 T^{n_I} Y_F \exp\left(-\frac{T_{aI}}{T}\right) \tag{1}$$

$$F + R \rightarrow 2R \qquad r_{II} = A_{II} \rho^2 T^{n_{II}} Y_F Y_R \exp\left(-\frac{T_{aII}}{T}\right) \tag{2}$$

$$R + M \rightarrow P + M(+q_c) \qquad r_{III} = A_{III} \rho^2 T^{n_{III}} Y_R \tag{3}$$

where F is the reactant, R is the radical, P is the product, M is the third body, q_c is the chemical heat release, r is the reaction rate, A is the Arrhenius constant, ρ is the density, T is the temperature, n is the temperature exponent, Y is the mass fraction, and T_a is the activation temperature. The first step is a chain-initiation reaction, which has high activation energy. It produces the initial radicals in the reactant stream and thus is critical to the autoignition process. The second step is a chain-branching reaction, which produces a massive number of radicals from the reactant at a certain temperature. It also has relatively high activation energy and is the dominant reaction during the flame propagation process. The last step is the radical termination reaction, which is insensitive to temperature. It converts radicals to the product and releases all chemical heat. The first reaction used to be neglected in analyses of classical laminar premixed flames. In the present study, the inlet reactant stream was considered reactive, and its chemical process was mimicked with the three reaction steps. In the following sections, the temperature exponent n was set to $n_{\mathrm{I}} = n_{\mathrm{II}} = n_{\mathrm{III}} = 2$ for the sake of simplicity [5]. This mechanism could qualitatively describe the high-temperature chemistry involved in autoignition and flame propagation (see Appendix A).

2.2. Model

Figure 1 shows the laminar lean premixed flame model considering pre-flame reactions. The flame was set to a semi-infinite one-dimensional domain. This work only considered the circumstances with weak autoignition tendencies, i.e., $Da_{ig} = \tau_f/\tau_{ig} \sim O(10^{-1})$, where $\mathrm{Da_{ig}}$ is the ignition Damkohler number [21]. So, the combustion process was still dominated by a diffusion-reaction balance mode. The presence of the pre-flame reaction gradually modified the reactant streamwise and assisted with the flame propagation. There were two sets of coordinates: one was defined as x with the origin at the flame front, where the radical concentration reached its maximum; the other was defined as ξ with the origin set at the flow inlet, which was upstream of the flame with the finite length L. The first coordinate was used to analyze the flame structure and steady-state propagation, while the second was used for the dynamic response to flow oscillation.

If the thermal (c_p) and transport ($\lambda,\ \rho D$) properties of the mixture were assumed constant, then the governing equations of the flame structure can be given as follows [5]:

$$\rho u = Const. \tag{4}$$

$$\rho u c_p \frac{dT}{dx} - \lambda \frac{d^2T}{dx^2} = q_c r_{III} \tag{5}$$

$$\rho u \frac{dY_F}{dx} - \rho D_F \frac{d^2Y_F}{dx^2} = \omega_F \tag{6}$$

$$\rho u \frac{dY_R}{dx} - \rho D_R \frac{d^2Y_R}{dx^2} = \omega_R \tag{7}$$

where u is the velocity, c_p is the specific heat, λ is the thermal conductivity, D is the mass diffusion coefficient, and ω is the mass production rate that satisfies $\omega_F = -r_I - r_{II}$ and $\omega_R = r_I + r_{II} - r_{III}$. The boundary conditions are

$$\begin{aligned} &T = T_u;\ Y_F = Y_{F,u};\ Y_R = 0,\ at\ x = -L \\ &T = T_b;\ Y_F = 0;\ Y_R = 0,\ at\ x \rightarrow +\infty \end{aligned} \tag{8}$$

The thermoacoustic behavior of a flame excited by inlet velocity fluctuation can be described as follows [19]. At a relatively low excitation frequency, a quasi-static assumption was employed because the reaction and scalar transportation reached a balance considerably faster than the velocity oscillation could:

$$\frac{d\xi_f}{dt} = u_{in}(t) - S\left(\xi_f\right) \tag{9}$$

$$p'(t) = u_{in}^{'}(t)\ Z \tag{10}$$

$$Q(t) = q_c Y_{F,u} \rho_u S\left(\xi_f\right) \tag{11}$$

where $u_{in} = \bar{u}_{in} + u'_{in}$ is the inlet velocity, $S(\xi_f)$ is the steady-state flame propagation speed for the flame front at the position ξ_f, p' is the pressure fluctuation, u'_{in} is the inlet velocity fluctuation, Z is the acoustic impedance, and Q is the heat release rate. The initial condition for this problem was set to a steady-state:

$$\xi_f = \xi_{f,0};\ u_{in,0} = S\left(\xi_{f,0}\right),\ \text{at } t = 0 \tag{12}$$

2.3. Analysis of the flame structure and its propagation

To simplify Eqs. (4)–(7), a set of non-dimensional variables was defined as follows:

$$\tilde{x} = \frac{\rho u c_p}{\lambda} x;\ \ \tilde{T} = \frac{c_p}{q_c Y_{F,u}} T;\ \ \tilde{Y}_F = \frac{Y_F}{Y_{F,u}};\ \ \tilde{Y}_R = \frac{Y_R}{Y_{F,u}} \tag{13}$$

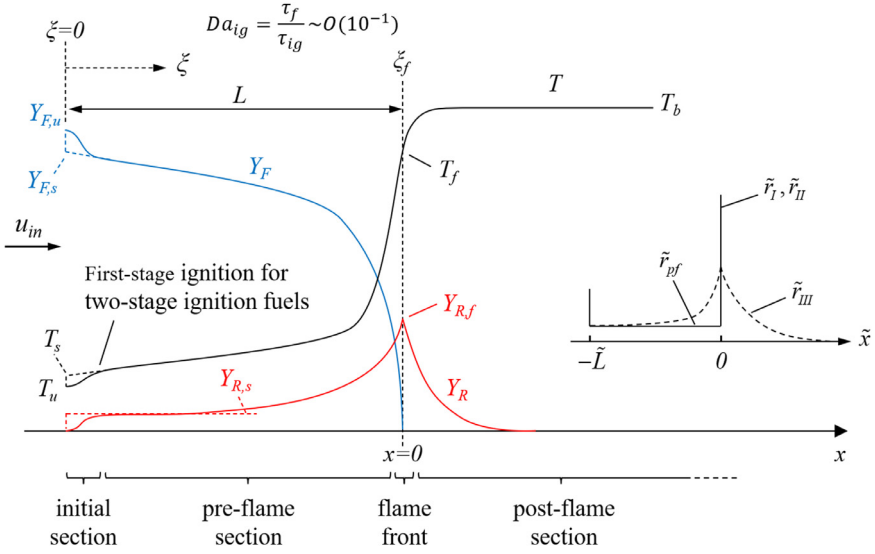

Fig. 1. Schematic of the flame structure under autoignitive conditions.

The non-dimensional governing equations are

$$\frac{d\tilde{T}}{d\tilde{x}}-\frac{d^2\tilde{T}}{d\tilde{x}^2}=Da_{III}\tilde{Y}_R \tag{14}$$

$$\frac{d\tilde{Y}_F}{d\tilde{x}}-\frac{1}{Le_F}\frac{d^2\tilde{Y}_F}{d\tilde{x}^2}=-Da_I\tilde{Y}_F\exp\left(-\frac{\tilde{T}_{aI}}{\tilde{T}}\right)-Da_{II}\tilde{Y}_F\ \tilde{Y}_R\exp\left(-\frac{\tilde{T}_{aII}}{\tilde{T}}\right) \tag{15}$$

$$\frac{d\tilde{Y}_R}{d\tilde{x}}-\frac{1}{Le_R}\frac{d^2\tilde{Y}_R}{d\tilde{x}^2}=Da_I\tilde{Y}_F\exp\left(-\frac{\tilde{T}_{aI}}{\tilde{T}}\right)+Da_{II}\tilde{Y}_F\ \tilde{Y}_R\exp\left(-\frac{\tilde{T}_{aII}}{\tilde{T}}\right)-Da_{III}\tilde{Y}_R \tag{16}$$

where Le is the Lewis number. Da is the Damkohler number and is defined as

$$Da_I=A_I\frac{p^2}{R_g^2}\frac{\lambda}{(\rho u)^2c_p}$$
$$Da_{II}=A_{II}\frac{p^2}{R_g^2}\frac{\lambda}{(\rho u)^2c_p}Y_{F,u}$$
$$Da_{III}=A_{III}\frac{p^2}{R_g^2}\frac{\lambda}{(\rho u)^2c_p} \tag{17}$$

where R_g represents the gas constant. The boundary conditions were converted to

$$\tilde{T}=\tilde{T}_u;\ \tilde{Y}_F=1;\tilde{Y}_R=0,\ \ at\ \tilde{x}=-\tilde{L} \tag{18}$$

$$\tilde{T}=\tilde{T}_b;\ \tilde{Y}_F=0;\tilde{Y}_R=0,\ \ at\ \tilde{x}=+\infty \tag{19}$$

The assumptions introduced to obtain an analytical solution were listed as follows.

(i) The flame structure of two-stage ignition fuels consisted of four sections, as shown in Fig. 1. In the initial section, the low-temperature chemistry initiated, causing the first-stage ignition. In the pre-flame section, the high-temperature chemistry gradually modulated the reactant mixture, causing a temperature increase and fuel consumption. In the flame front section, the chain-branching reaction quickly converted all remaining reactants into radicals. In the post-flame section, the radicals were burnt, and the combustion process was completed.

(ii) The first-stage ignition was modeled as a jump condition (shown below) immediately downstream the flow inlet since the three-step mechanism could not describe it.

$$\tilde{T}=\tilde{T}_u;\ \tilde{Y}_F=1;\tilde{Y}_R=0;\tilde{Y}_P=0,\ \ at\ \tilde{x}=\left(-\tilde{L}\right)^-$$
$$\tilde{T}=\tilde{T}_s;\ \tilde{Y}_F=\tilde{Y}_{F,s};\tilde{Y}_R=\tilde{Y}_{R,s};\tilde{Y}_P=\tilde{Y}_{P,s},\ \ at\ \tilde{x}=\left(-\tilde{L}\right)^+ \tag{20}$$

where the parameters satisfy the following relationships:

$$\tilde{Y}_{F,s}+\tilde{Y}_{R,s}+\tilde{Y}_{P,s}=1$$
$$\tilde{T}_s-\tilde{T}_u=\tilde{Y}_{P,s}$$
$$Da_I\tilde{Y}_{F,s}\exp\left(-\frac{\tilde{T}_{aI}}{\tilde{T}_s}\right)+Da_{II}\tilde{Y}_{F,s}\tilde{Y}_{R,s}\exp\left(-\frac{\tilde{T}_{aII}}{\tilde{T}_s}\right)=Da_{III}\tilde{Y}_{R,s} \tag{21}$$

This assumption neglected the induction length of the first-stage ignition. It might not be suitable in other cases.

(iii) The reaction rate in the pre-flame section was constant because the heat release and fuel consumption here were limited. The reaction rate could be estimated as

$$r_{pf}=A_I\frac{p^2}{R_g^2}Y_{F,s}\exp\left(-\frac{T_{aI}}{T_s}\right)+A_{II}\frac{p^2}{R_g^2}Y_{F,s}Y_{R,s}\exp\left(-\frac{T_{aII}}{T_s}\right)=A_{III}\frac{p^2}{R_g^2}Y_{R,s}$$
$$\tilde{r}_{pf}=Da_I\tilde{Y}_{F,s}\exp\left(-\frac{\tilde{T}_{aI}}{\tilde{T}_s}\right)+Da_{II}\tilde{Y}_{F,s}\tilde{Y}_{R,s}\exp\left(-\frac{\tilde{T}_{aII}}{\tilde{T}_s}\right)=Da_{III}\tilde{Y}_{R,s} \tag{22}$$

based on the assumption (ii).

(iv) The flame front was modeled as a thin reaction sheet; in other words, the chain-branching reaction was fast enough to convert all remaining reactants into radicals at $x=0$. Thus, the jump condition [22,23] across the flame front was

$$\left[\tilde{T}\right]_{\tilde{x}=0^-}^{\tilde{x}=0^+}=\left[\tilde{Y}_F\right]_{\tilde{x}=0^-}^{\tilde{x}=0^+}=\left[\tilde{Y}_R\right]_{\tilde{x}=0^-}^{\tilde{x}=0^+}=\left[\frac{d\tilde{T}}{d\tilde{x}}\right]_{\tilde{x}=0^-}^{\tilde{x}=0^+}$$
$$=\left[\frac{1}{Le_F}\frac{d\tilde{Y}_F}{d\tilde{x}}+\frac{1}{Le_R}\frac{d\tilde{Y}_R}{d\tilde{x}}\right]_{\tilde{x}=0^-}^{\tilde{x}=0^+}=0 \tag{23}$$

(v) The Lewis number of the radical was unity, i.e., $Le_R=1$.

(vi) The non-dimensional length of the pre-flame section was much larger than unity, i.e., $\tilde{L}\gg 1$.

Therefore, an explicit solution for the flame propagation speed (S) could be obtained (see Appendix B) as

$$S=2T_u\frac{T_b-T_f}{T_b-T_s}\sqrt{A_{III}\frac{\lambda}{c_p}}+\frac{T_b-T_u}{T_b-T_s}\frac{r_{pf}L}{Y_{F,u}\rho_u} \tag{24}$$

Table 1
Non-dimensional parameter setting.

$\tilde{L}$	30.0	$\tilde{T}_u$	0.7056
Le_F	3.479	$\tilde{T}_f$	1.633
Le_R	1.0		

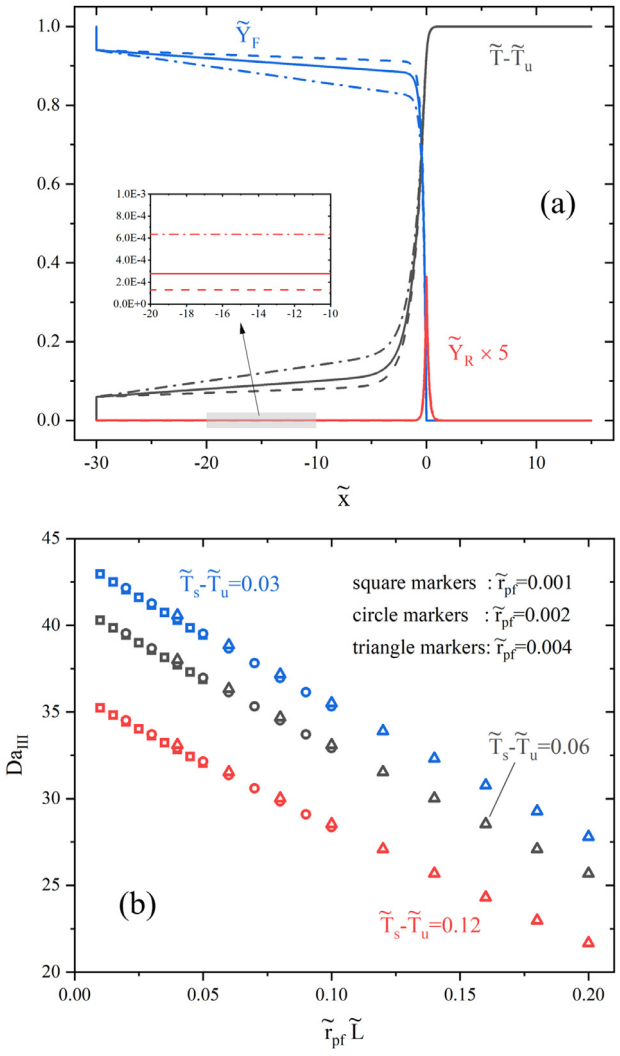

Fig. 2. Analytical solution of a flame under autoignitive conditions: (a) flame structure (dashed lines: $\tilde{r}_{pf} = 0.001$ and $\tilde{T}_s - \tilde{T}_u = 0.03$; solid lines: $\tilde{r}_{pf} = 0.002$ and $\tilde{T}_s - \tilde{T}_u = 0.06$; dash-dot lines: $\tilde{r}_{pf} = 0.004$ and $\tilde{T}_s - \tilde{T}_u = 0.12$; dotted lines: analytical solution without considering pre-flame reactions); (b) Damkohler number.

The first term, which is approximate to $\sqrt{\lambda/c_p}$, is the flame propagation speed without considering the pre-flame reactions in the pre-flame section. This suggested that the first-stage ignition in the initial section (T_s) could also lead to flame speed acceleration. The second term, which is approximate to $\frac{r_{pf}L}{T_b - T_s}$, indicated that the flame speed was linearly related to its spatial location and that the gradient of this relationship was amplified by the pre-flame reactions occurring in the initial section.

Flame structure examples according to Eqs. (43), (44), and (46), along with the solution without considering pre-flame reactions (i.e., the dotted lines), were drawn in Fig. 2(a). The non-dimensional parameters were set as shown in Table 1. These results suggested that the non-dimensional thickness of the high-temperature flame was not affected by the temperature increase and fuel consumption caused by pre-flame reactions in front of it. The radical concentration profiles were identical at the flame front for all four cases. In the range $\tilde{x} < -5$, the diffusion transport of the flame was negligible, and a pre-flame reaction-convection balance was established. The non-dimensional fuel concentration and temperature profiles showed good linearity, as described by the term $\tilde{r}_{pf}\tilde{x}$ in Eqs. (43) and (46). The non-dimensional mass fraction of radicals was in the order of 10^{-4} in this section, which increased as the pre-flame reaction rate increased. Fig. 2(b) shows the dependence of the Damkohler number (Da_{III}) on the accumulation of pre-flame reactions occurring in the pre-flame section. Three pre-flame reaction rates (0.001, 0.002 and 0.004) and three initial temperature increases (0.03, 0.06 and 0.12) were chosen for the calculations with $\tilde{L} = 10 - 50$. These results showed that Da_{III} decreased linearly as the pre-flame reactions accumulated in the initial and pre-flame sections. The effects of the nonlinear terms in Eq. (51) were imperceptible.

2.4. Analysis of the thermoacoustic behavior

The thermoacoustic behavior of the flame under autoignitive conditions was examined by introducing a simple harmonic velocity oscillation to the inlet:

$$\frac{u_{in}(t)}{u_{in,0}} = 1 + A\sin(2\pi f t) \tag{25}$$

where A is the relative amplitude and f is the frequency. The movement of the flame front could be obtained numerically by substituting the solutions of Eqs. (48) and (49) into Eq. (9). For convenient analysis, a linear approximation was employed to describe the relationship between the flame speed and its position:

$$S(\xi_f) = S(\xi_{f,0}) + k(\xi_f - \xi_{f,0}) \tag{26}$$

where k is a coefficient (unit: s^{-1}). Numerical simulations suggested that k is a positive number and increases with ξ_f. Therefore, the flame movement yields

$$\frac{d\xi_f}{dt} = u_{in,0}A\sin(2\pi f t) - k(\xi_f - \xi_{f,0}) \tag{27}$$

and its solution is

$$\xi_f = \xi_{f,0} + \frac{2\pi f}{(2\pi f)^2 + k^2}u_{in,0}Ae^{-kt} + \frac{u_{in,0}A}{\sqrt{(2\pi f)^2 + k^2}}\sin(2\pi f t - \phi) \tag{28}$$

where $\phi = \tan^{-1}(\frac{2\pi f}{k}) \in (0, \frac{\pi}{2})$ is the phase delay. If the flame propagation speed was considered as a constant (i.e., $k = 0$), the flame movement yields

$$\xi_f = \xi_{f,0} + \frac{u_{in,0}A}{2\pi f} + \frac{u_{in,0}A}{2\pi f}\sin\left(2\pi f t - \frac{\pi}{2}\right) \tag{29}$$

The impact of the pre-flame reactions on the flame front movement could be determined by comparing the solutions of Eqs. (28) and (29). Under autoignitive conditions, the equilibrium position of the flame oscillation could return to the initial position because of $k > 0$. Second, the amplitude of the steady-state oscillation could be reduced. Third, the phase difference between the flame oscillation and velocity excitation could be altered by the pre-flame reactions.

Substituting Eq. (11) into the solution of Eq. (28) yields the heat release rate with velocity fluctuation:

$$\frac{Q(t)}{Q_0} = 1 + \frac{2\pi fkA}{(2\pi f)^2 + k^2}e^{-kt} + \frac{kA}{\sqrt{(2\pi f)^2 + k^2}}\sin(2\pi f t - \phi) \tag{30}$$

where Q_0 is the heat release rate at $t = 0$. For $t \to \infty$ and oscillation reaching a steady-state, the fluctuation of the heat release rate

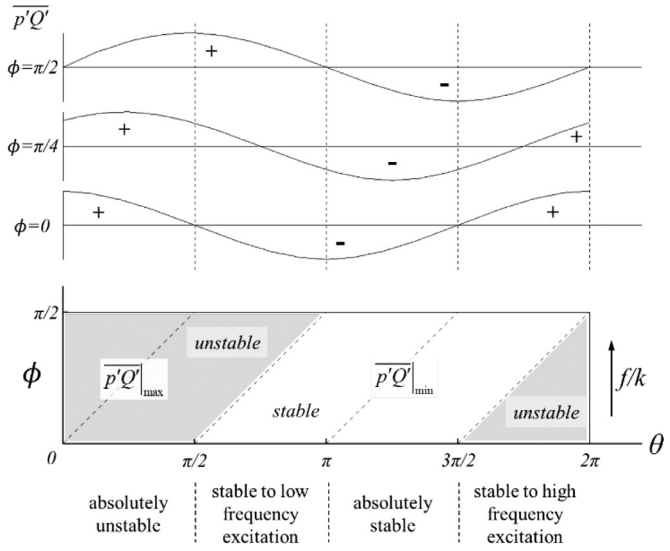

Fig. 3. Thermoacoustic stability diagram of a flame under autoignitive conditions.

is given as

$$Q'(t) = Q_0 \frac{kA}{\sqrt{(2\pi f)^2 + k^2}} \sin(2\pi f t - \phi) \tag{31}$$

This can also be given in the form of an n-τ model [24]:

$$Q'(t) = n\, u'_{in}(t-\tau) \tag{32}$$

where

$$n = \frac{q_c Y_{F,u} \rho_u}{\sqrt{\left(\frac{2\pi f}{k}\right)^2 + 1}};\quad \tau = \frac{1}{2\pi f} \tan^{-1}\left(\frac{2\pi f}{k}\right) \tag{33}$$

Combining Eqs. (25) and (31) obtains the flame transfer function of a planar premixed flame under autoignitive conditions:

$$FTF = \frac{\widehat{Q'}(\omega)/\bar{Q}}{\widehat{u'_{in}}(\omega)/\overline{u_{in}}} = \frac{k}{\sqrt{\omega^2 + k^2}} e^{-j\phi} \tag{34}$$

where $\omega = 2\pi f$ is the angular frequency and j is an imaginary unit.

For a planar wave, the acoustic impedance is constant to a spatial location and may be expressed as

$$Z = \rho_u c_u e^{-j\theta} \tag{35}$$

where c_u is the sound speed of the reactant and $\theta \in [0, 2\pi)$ is the phase difference between the velocity and pressure oscillation [25]. Therefore, the steady-state pressure oscillation yields

$$p'(t) = \rho_u c_u u_{in,0} A \sin(2\pi f t - \theta) \tag{36}$$

The Rayleigh criterion for this thermoacoustic behavior is

$$\overline{p'Q'} = f \int_0^{1/f} p'(t) Q'(t) dt = \frac{\rho_u c_u u_{in,0} Q_0 A^2}{2\sqrt{\left(\frac{2\pi f}{k}\right)^2 + 1}} \cos(\theta - \phi) \tag{37}$$

A schematic diagram of this criterion is shown in Fig. 3. It indicated that the stability of a planar flame to velocity excitation depends on both θ and ϕ. Furthermore, it was controlled by the coefficient k, which represented the impact of the pre-flame reactions on flame propagation, and the acoustic impedance Z, which represented the characteristics of the acoustic environment. The figure showed that, when the effect of thermoacoustic coupling reached its maximum at $\theta = \phi$, the pressure oscillation was rapidly amplified. The system was most stable at $\theta = \phi + \pi$, and any pressure fluctuation was damped swiftly. Moreover, there were four stability scenarios for certain acoustic environments. For $\theta \in [0, \frac{\pi}{2}]$, the flame was absolutely unstable to all excitations. For $\theta \in (\frac{\pi}{2}, \pi)$, the flame was stable to excitation frequencies lower than $\frac{k}{2\pi}\tan(\theta - \frac{\pi}{2})$. This meant that, under such circumstances, the combustion process might emit high-frequency noises. For $\theta \in [\pi, \frac{3\pi}{2})$, the flame was stable for all excitations that were usually most desired in engineering applications. For $\theta \in [\frac{3\pi}{2}, 2\pi)$, the flame was unstable to low-frequency excitations. Because ϕ depended on both f and k, Eq. (37) also suggested that, if $\theta \in (\frac{\pi}{2}, \pi)$ or $(\frac{3\pi}{2}, 2\pi)$, the stability of the flame at a certain excitation frequency could change depending on the operating conditions.

Table 2
Parameters for the theoretical model.

		Methane	DME	Diesel
$Y_{F,u}$	–	0.03384	0.06285	0.03946
q_c	J/kg	4.473×10^7	2.597×10^7	3.722×10^7
c_p	J/kg•K	1207	1212	1205
λ	W/m•K	0.0832	0.0850	0.0825
Le_F	–	0.97	1.665	3.479
Le_R	–	1.0	1.0	1.0
T_f	K	2050	2074	1990
T_s	K	860	918.4	926.2

3. Numerical simulation

3.1. Setup

A series of numerical simulations were conducted to validate the analysis in Section 2. The operating pressure, inlet temperature, and equivalence ratio were 3 MPa, 860 K, and 0.6, respectively. A binary mixture of n-dodecane (77 vol%) and m-xylene (23 vol%) was chosen as a surrogate fuel for diesel [26,27].

One-dimensional, transient, and isobaric Navier–Stokes equations were chosen as the governing equations. The fourth-order conservative scheme [28] and optimal third-order total variation diminishing (TVD) Runge–Kutta method [29] were employed for spatial and temporal discretization, respectively. Open-source Cantera modules were used to evaluate the transport and reaction terms. A skeletal mechanism [27] consisting of 163 species and 887 reactions was employed to predict the propagation behavior of the lean premixed flame under autoignitive conditions. The length of the computational domain was 1 mm for most cases. The spatial and temporal resolutions were 5×10^{-7} m and 10^{-7} s, respectively.

Table 2 presents the parameters of the analytical model. The transport properties were determined at the mean temperatures of T_u and T_b. The Lewis number of methane, dimethyl ether (DME), and surrogate diesel fuel was set as suggested by van Oijen [30], Deng et al. [31], and Vié et al. [32], respectively.

3.2. Flame structure and its steady-state propagation

Figure 4 shows the steady-state flame structure at various anchor positions. The flame was still dominated by a diffusion-reaction balance under autoignitive conditions. The pre-flame reaction was notable for causing a small temperature rise and modifying the reactant stream in front of the high-temperature reaction zone, which accelerated the flame propagation.

The analytical solution (dashed lines) captured some of the main features of the flame structure that were predicted by the numerical simulation (solid and dash-dot lines). First, the first-stage ignition initiated immediately downstream the flow inlet,

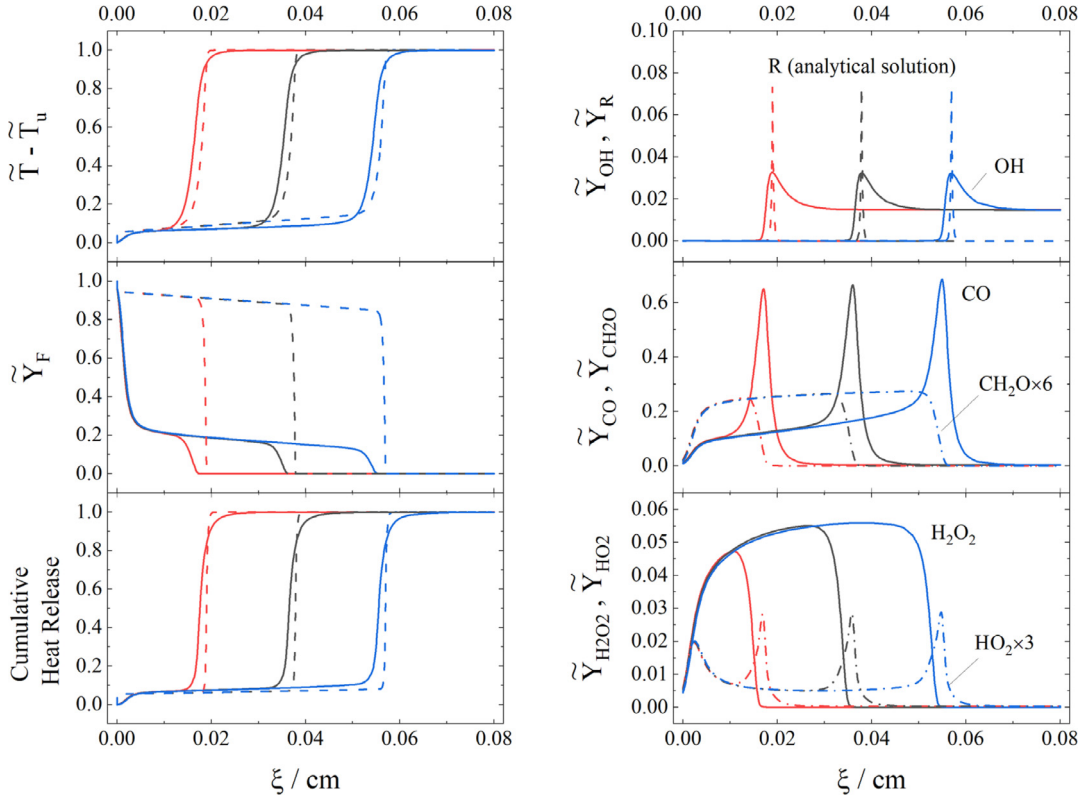

Fig. 4. Flame structure under autoignitive conditions (solid and dash-dot lines: numerical simulations; dashed lines: analytical solutions).

the length of which was less than 0.005 cm. This scale and the reaction path inside this section were unaffected by the anchor position or propagation speed of the flame. Second, in the region upstream of the flame front, the profile of the temperature, fuel concentration, and cumulative heat release showed good linearity. A constant spatial distribution was observed for the concentration of minor species, some of which were critical to the pre-flame reactions (e.g., OH, CH_2O, and H_2O_2). This indicated that, in this region, the pre-flame reaction rate was close to a constant value, which agreed with the theoretical analysis. Third, for the minor species related to high-temperature chemistry (e.g., OH, CO, and HO_2), the peak value of the mass fraction profile was constant with the anchor position of the flame front. This verified the analytical solution of Eq. (50).

Because of the lack of complexity in the chemical kinetics, the analysis had two major limitations. First, a considerable amount (up to 75%) of fuel was decomposed into smaller alkyl radicals inside the initial section due to low-temperature chemistry; however, the increase in temperature in this section was only about 66 K, which was 5.8% of the total temperature rise. This phenomenon could not be depicted by the three-step mechanism. Second, the flame predicted by the analysis was much thinner than that predicted by the numerical simulation with the skeletal or the three-step mechanism (Fig. 11). This was because of the thin reaction sheet assumption (i.e., Eq. (23)), which took the thickness of the reaction layer as infinitesimal and overestimated the reaction rate of high-temperature chemistry.

Figure 5 shows the dependence of the flame propagation speed on the pre-flame length. For the right ordinate, τ_{ig} is the autoignition delay time, which was 1.826 ms in the present case. τ_f is the pre-flame flow residence time and is defined as

$$\tau_f = \int_0^{\xi_f} \frac{d\xi}{u(\xi)} \tag{38}$$

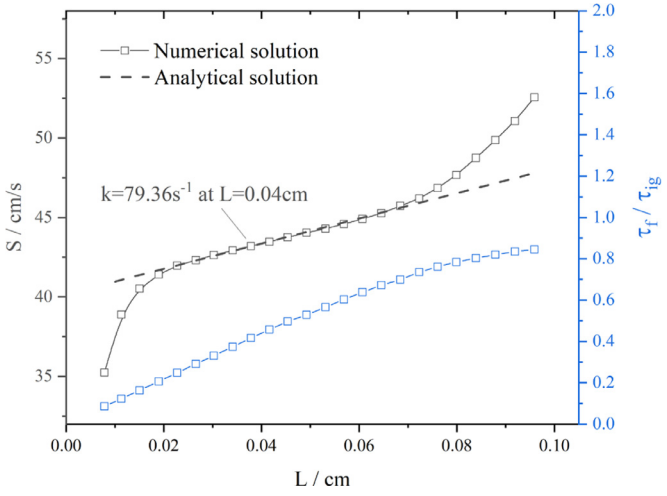

Fig. 5. Dependence of the flame speed on the pre-flame length.

where $u(\xi)$ is the axial velocity profile. In the range of $\tau_f / \tau_{ig} = 0.2$–0.6, the flame speed predicted by the numerical simulation showed good linearity with the pre-flame length, which agreed well with the theoretical analysis. When $\tau_f / \tau_{ig} < 0.2$, the flame speed dropped dramatically as the pre-flame length decreased. This might be because of the heat loss from the flame to flow inlet by diffusion because the pre-flame length was so short. At $\tau_f / \tau_{ig} > 0.6$, the combustion behavior was gradually dominated by the autoignition process. A convection–reaction balance gradually formed at the high-temperature chemistry front, and the slope of the flame speed curve increased rapidly.

Two other fuels, methane and DME, were included to further validate the theoretical analysis, the parameters of which are

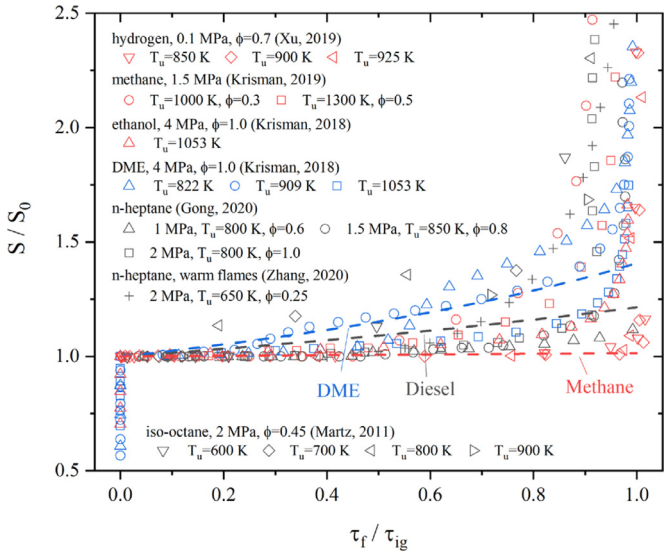

Fig. 6. Dependence of the normalized flame speed on the normalized residence time (dashed lines: analytical solutions at 3 MPa, T_u=860 K, ϕ=0.6).

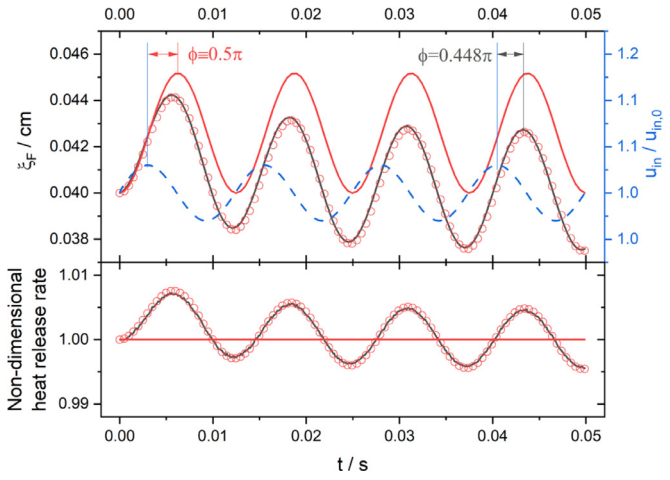

Fig. 7. Dynamic response of the flame to inlet velocity fluctuation (black solid lines: numerical simulation results; red circle markers: analytical solution considering pre-flame reactions; red solid lines: analytical solution without considering pre-flame reactions; blue dashed line: velocity modulation).

shown in Table 2. Figure 6 shows the dependence of the normalized flame speed on the normalized residence time, where the analytical solution was roughly estimated as

$$\frac{S}{S_0} = \frac{T_b - T_s}{T_b - T_s \exp\left[\frac{R_g q_c \tau_{ig} r_{pf}}{p c_p}\left(\tau_f/\tau_{ig}\right)\right]} \tag{39}$$

under the assumptions (i)-(vi). Despite differences in fuel and operating conditions, the analytical solutions agreed well with the existing literature ([10–14, 21]) when $\tau_f / \tau_{ig} < 0.6$. In general, the flame acceleration was most notable for DME at low τ_f / τ_{ig} before the curve reaching the turning point, while it was neglectable for fuels with single-stage ignition, e.g., hydrogen, methane, and ethanol.

3.3. Flame oscillation with inlet velocity fluctuation

Figure 7 shows the dynamic response of the flame to inlet velocity fluctuation in the numerical simulation. The frequency of the inlet velocity excitation was set to 80 Hz, which was the "growl" frequency in a lean premixed prevaporized (LPP) combustor [33].

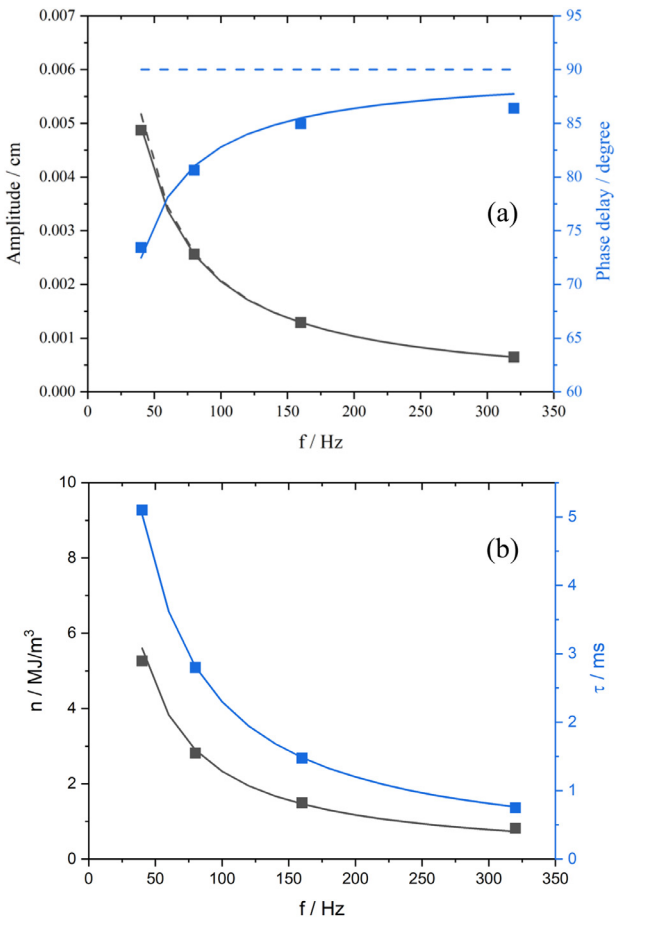

Fig. 8. Flame oscillation at various excitation frequencies (square markers: numerical simulation results; solid lines: analytical solution considering pre-flame reactions; dashed lines in (a): analytical solution without considering pre-flame reactions).

The relative amplitude of the fluctuation was set to 3%, which was low enough to avoid any nonlinear behavior that would be beyond the scope of this study. In the present numerical simulation, the pressure was considered as spatially and temporally constant. Therefore, the complex nature of thermoacoustic coupling was not considered here. Figure 7 shows that the inlet velocity excitation caused the position of the flame front and the heat release rate to oscillate with the same frequency. The simulation results, which considered the skeletal reaction mechanism, agreed well with the analytical solution based on the linear approximation in Eq. (26). The equilibrium position of the flame returned to the initial position within three cycles, and the phase delay of the flame oscillation relative to the velocity fluctuation was about 0.448π; this was smaller than the phase delay that did not consider the impact of pre-flame reactions on the flame propagation.

Numerical simulations were also performed with excitation frequencies of 40, 160, and 320 Hz. The results are shown in Fig. 8. The simulation results agreed well with the theoretical analysis. The amplitude of the flame oscillation dropped as the excitation frequency increased, and the impact of the pre-flame reactions on this parameter was exceedingly small in the high-frequency section. With increasing frequency, the phase delay of the flame fluctuation increased and gradually approached $\pi/2$, which was the value for the case not considering pre-flame reactions. The results showed that both n and τ decreased with increasing frequency.

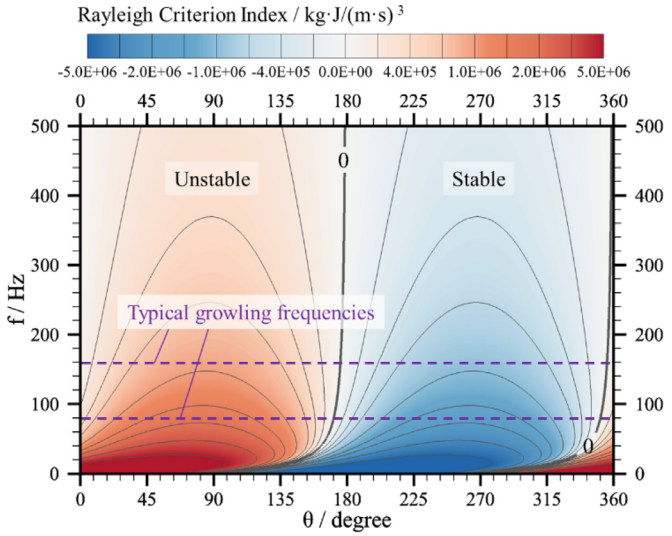

Fig. 9. Contours of the Rayleigh criterion index.

3.4. Thermoacoustic behavior

Figure 9 shows the contours of the Rayleigh criterion index, which were calculated according to Eq. (37) at $k = 79.36\ s^{-1}$. These contours embodied the thermoacoustic stability diagram in Fig. 3. Above 80 Hz, the stable and unstable regions were roughly separated by the lines of $\theta = \pi$ and $\theta = 2\pi$ because k was relatively small. At low frequencies, however, the situation was much complex. The boundaries between the stable and unstable regions were strongly nonlinear. The scenario of selective filtering (see Section 2.4) could occur if $\theta = \pi/2–\pi$ or $\theta = 3\pi/2–2\pi$. The value of the Rayleigh criterion index fluctuated along the θ direction, and the amplitude of this fluctuation dropped rapidly along the f direction.

4. Conclusions

To address engineering challenges encountered in developing advanced gas turbine combustors, theoretical analysis and numerical simulation were performed to investigate the thermoacoustic instability of a laminar lean premixed flame under autoignitive conditions. The major conclusions were as follows:

(1) The three-step mechanism employed by analysis could qualitatively describe the high-temperature chemistry involved in autoignition and flame propagation, while the behavior of the first-stage ignition was missing.

(2) The typical structure of a lean premixed flame burning two-stage ignition fuels under autoignitive conditions consisted of four sections. In the initial section, the low-temperature chemistry initiated, causing the first-stage ignition. In the pre-flame section, many radicals reached the steady-state, and the fuel consumption rate and heat release rate were constant. In the flame front, the rate of high-temperature chain-branching chemistry reached its maximum. In the post-flame section, the combustion process gradually reached completion.

(3) The results from the theoretical analysis and numerical simulation indicated that the propagation speed of a flame under autoignitive conditions was affected by the accumulation of pre-flame reactions, which was related to the spatial location of the flame front. Under certain conditions (e.g., $\tau_f / \tau_{ig} = 0.2–0.6$), the flame speed showed a linear correlation with the pre-flame length.

(4) The flame oscillation, which was excited by the inlet velocity, was investigated. The results suggested that, under autoignitive conditions, the pre-flame reactions could cause the equilibrium position of the flame oscillation to return to the initial position and could alter the phase delay.

(5) The thermoacoustic behavior of a planar flame was evaluated according to the Rayleigh criterion. The stability diagram and contours of the Rayleigh criterion index revealed that, under autoignitive conditions, a new mechanism for thermoacoustic instability might emerge because the overall heat release rate might be associated with the spatial location of the flame front. The flame might amplify, damp, high-pass filter, or low-pass filter the acoustic energy based on the phase difference between the velocity and pressure oscillations.

The findings from this study could contribute to the improvement of combustion models in CFD simulations. The constraint for inhibiting the thermoacoustic instability (i.e., $\theta \in [\pi, \frac{3\pi}{2})$) might also prove useful in optimizing the design of advanced gas turbine combustors. The limitations of this work, such as some of the assumptions employed in the analysis and the absence of compressibility in the numerical simulations, will be addressed in future research.

Acknowledgments

Funding: This work was supported by the National Natural Science Foundation of China (51406200).

Declaration of Competing Interest

The authors declare that they have no known competing financial interests or personal relationships that could have appeared to influence the work reported in this paper.

Appendix

Appendix A

Table 3 presents the parameters of the three-step mechanism. Three fuels, i.e., methane, DME, and surrogate diesel fuel (77 vol% n-dodecane + 23 vol% m-xylene), were included representing small hydrocarbon with single-stage ignition, small hydrocarbon with two-stage ignition, and large hydrocarbon with two-stage ignition, respectively. A unified activation temperature (T_{aI}) was chosen for all fuels, the value of which corresponded to E_a=30 kcal/mol [34]. The activation temperature (T_{aII}) was set as the flame temperature (T_f). The Arrhenius constant (A_{III}) was tuned to fit the flame speed to the prediction with detailed or skeletal mechanisms. Other Arrhenius constants, A_I and A_{II}, were set to reproduce the ignition delay time as much as possible.

To validate the adequacy of the three-step mechanism in depicting autoignition assisted flames, the CHEMKIN codes of PSR and PREMIX were employed with mechanisms developed by Smith et al. [35], Zhao et al. [36], and Pei et al. [27], respectively. The same operating condition as in Section 3 was chosen for all cases. Analytical solutions were also acquired for comparison, the parameters of which were shown in Table 2.

Table 3
Parameters of the three-step mechanism.

		Methane	DME	Diesel
A_I	$m^3/kg•s•K^2$	0.1149	385.0	107.4
T_{aI}	K	15,105	15,105	15,105
A_{II}	$m^3/kg•s•K^2$	0.08842	0.04914	0.03236
T_{aII}	K	2050	2074	1990
A_{III}	$m^3/kg•s•K^2$	0.2758	0.3087	0.1409

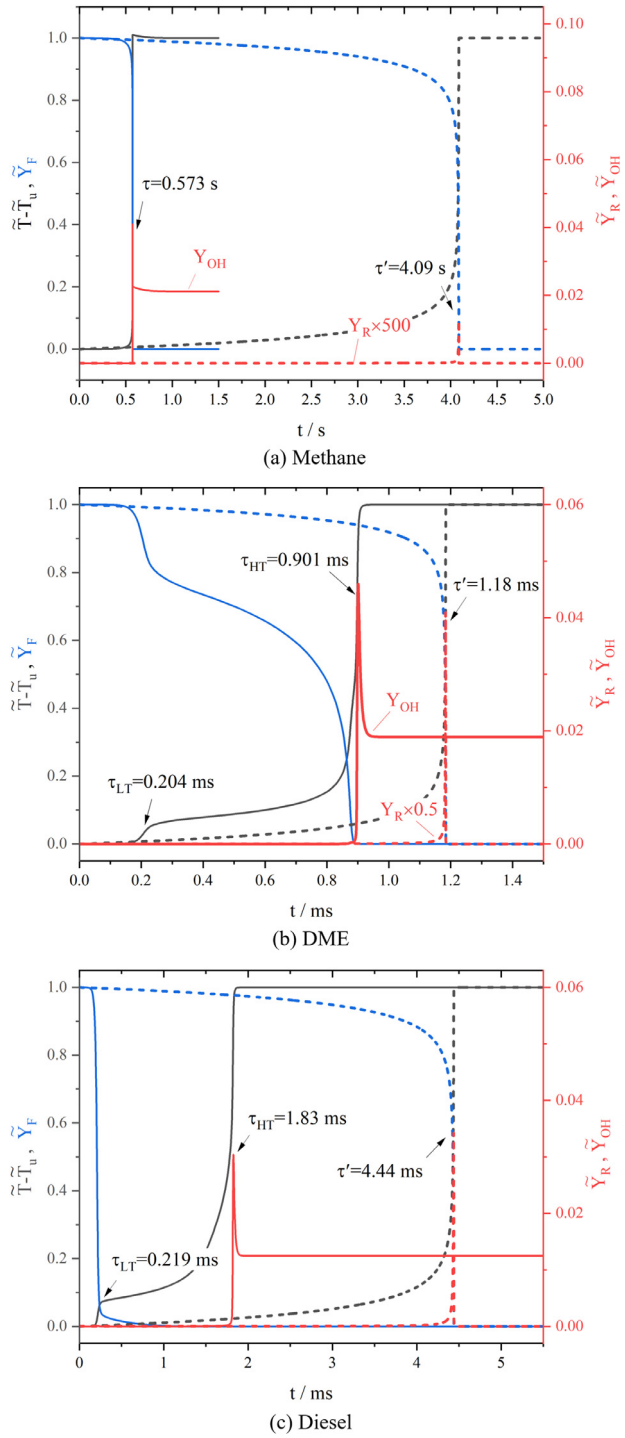

Fig. 10. Computed scalar profiles in a perfectly stirred reactor (solid lines: detailed or skeletal mechanism results; dashed lines: the three-step mechanism results).

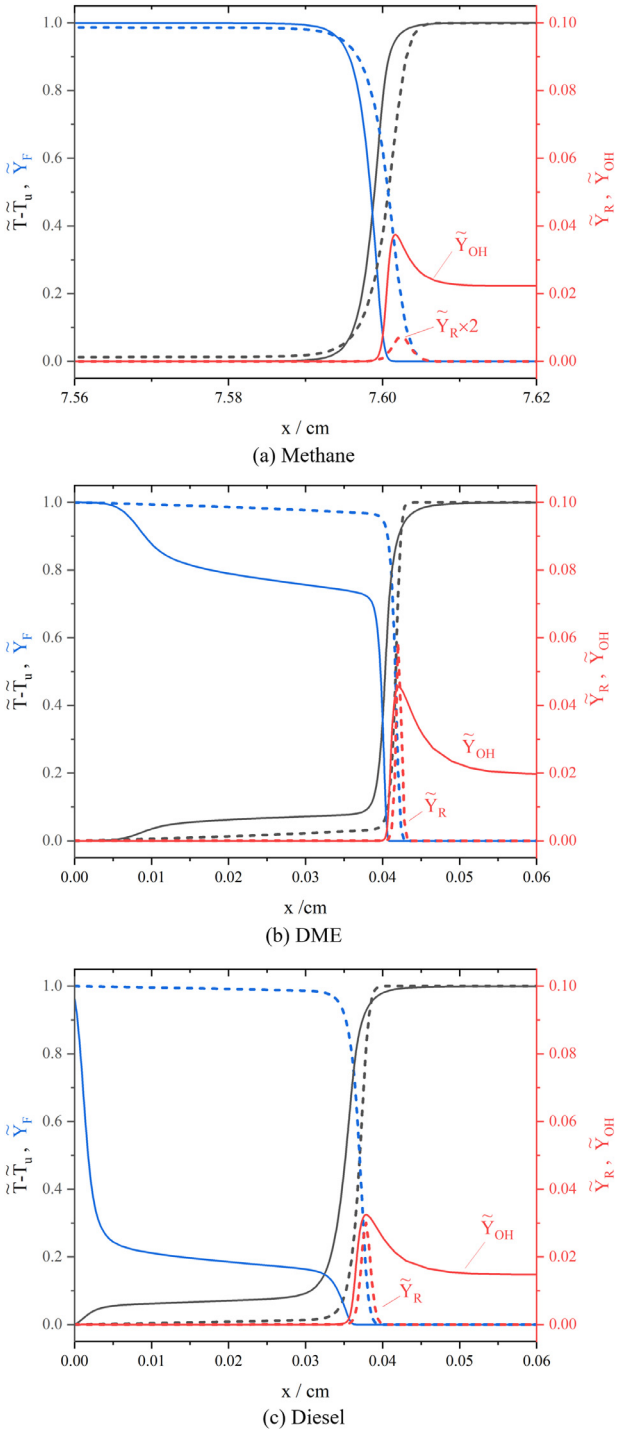

Fig. 11. Computed flame structure (solid lines: detailed or skeletal mechanism results; dashed lines: the three-step mechanism results).

The numerical results shown in Figs. 10, 11 and 12 indicated that the three-step mechanism could qualitatively describe the autoignition and flame propagation process. However, due to its simplicity, the deviation in predicting ignition delay times could be as large as 7 times for methane. And the deviation in predicting flame speeds could be as large as 70% for DME. Furthermore, the three-step mechanism could not describe the low-temperature chemistry. The behavior of the first stage ignition was missing.

Appendix B

Under assumptions (i)-(iv), the governing equations and their boundary conditions can be written as

$$\frac{d\tilde{T}}{d\tilde{x}} - \frac{d^2\tilde{T}}{d\tilde{x}^2} = Da_{III}\tilde{Y}_R$$
$$\left[\tilde{T}\big|_{\tilde{x}=(-\tilde{L})^+} = \tilde{T}_s;\ \tilde{T}\big|_{\tilde{x}=0} = \tilde{T}_f;\ \tilde{T}\big|_{\tilde{x}\to+\infty} = \tilde{T}_b\right] \quad (40)$$

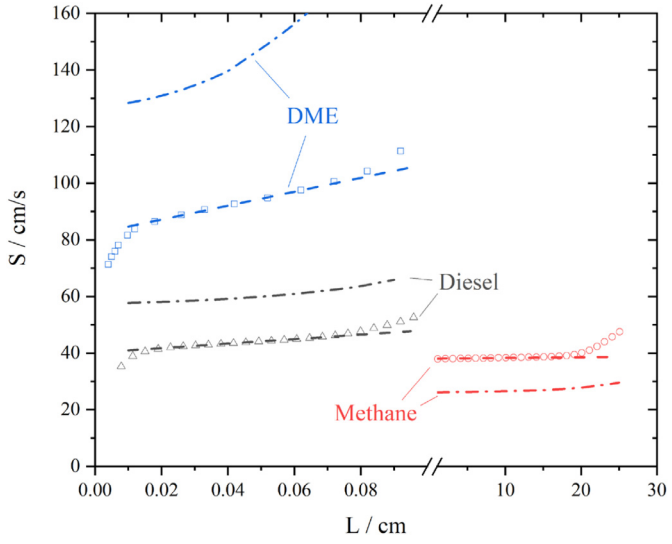

Fig. 12. Dependence of the flame speed on the pre-flame length (markers: detailed or skeletal mechanism results; dash-dot lines: the three-step mechanism results; dashed lines: analytical solutions).

$$\begin{cases} \frac{d\tilde{Y}_F}{d\tilde{x}} - \frac{1}{Le_F}\frac{d^2\tilde{Y}_F}{d\tilde{x}^2} = -\tilde{r}_{pf} & (\tilde{x} < 0) \\ \tilde{Y}_F = 0 & (\tilde{x} > 0) \end{cases}$$
$$\left[\tilde{Y}_F\big|_{\tilde{x}=(-\tilde{L})^+} = \tilde{Y}_{F,s};\ \tilde{Y}_F\big|_{\tilde{x}=0} = 0\right] \quad (41)$$

$$\begin{cases} \frac{d\tilde{Y}_R}{d\tilde{x}} - \frac{1}{Le_R}\frac{d^2\tilde{Y}_R}{d\tilde{x}^2} = \tilde{r}_{pf} - Da_{III}\tilde{Y}_R & (\tilde{x} < 0) \\ \frac{d\tilde{Y}_R}{d\tilde{x}} - \frac{1}{Le_R}\frac{d^2\tilde{Y}_R}{d\tilde{x}^2} = -Da_{III}\tilde{Y}_R & (\tilde{x} > 0) \end{cases}$$
$$\left[\tilde{Y}_R\big|_{\tilde{x}=(-\tilde{L})^+} = \tilde{Y}_{R,s};\ \tilde{Y}_R\big|_{\tilde{x}=0} = \tilde{Y}_{R,f};\ \tilde{Y}_R\big|_{\tilde{x}\to+\infty} = 0\right] \quad (42)$$

where T_f and $Y_{R,f}$ are the temperature and radical mass fraction, respectively, at the flame front, as shown in Fig. 1. These parameters were determined by the chemical, thermal, and transport properties of the mixture at which the chain-branching rate became equal to the rate of removal of radicals by molecular diffusion [22,23].

The profile of the reactant mass fraction is obtained by solving Eq. (41) as follows:

$$\tilde{Y}_F = -\tilde{r}_{pf}\tilde{x} + \frac{\tilde{Y}_{F,s} - \tilde{r}_{pf}\tilde{L}}{1 - \exp\left(-Le_F\tilde{L}\right)}\left[1 - \exp\left(Le_F\tilde{x}\right)\right],\ \tilde{x} < 0 \quad (43)$$

The profile of the radical mass fraction is obtained by solving Eq. (42) as follows:

$$\tilde{Y}_R = \begin{cases} C_1\exp\left(\alpha_1\tilde{x}\right) + C_2\exp\left(\alpha_2\tilde{x}\right) + \tilde{Y}_{R,s} & (\tilde{x} < 0) \\ \tilde{Y}_{R,f}\exp(\alpha_2\tilde{x}) & (\tilde{x} > 0) \end{cases} \quad (44)$$

where α_1, α_2, C_1 and C_2 are constants:

$$\alpha_{1,2} = \frac{Le_R \pm \sqrt{Le_R^2 + 4Le_R Da_{III}}}{2}$$
$$C_1 = \frac{-\left(\tilde{Y}_{R,f} - \tilde{Y}_{R,s}\right)\exp\left(-\alpha_2\tilde{L}\right)}{\exp\left(-\alpha_1\tilde{L}\right) - \exp\left(-\alpha_2\tilde{L}\right)}$$
$$C_2 = \frac{\left(\tilde{Y}_{R,f} - \tilde{Y}_{R,s}\right)\exp\left(-\alpha_1\tilde{L}\right)}{\exp\left(-\alpha_1\tilde{L}\right) - \exp\left(-\alpha_2\tilde{L}\right)} \quad (45)$$

By substituting Eq. (44) into Eq. (40), the temperature profile yields

$$\tilde{T} = \begin{cases} C_3\exp(\tilde{x}) + C_4 + \beta_1\exp(\alpha_1\tilde{x}) + \beta_2\exp(\alpha_2\tilde{x}) + \tilde{r}_{pf}\tilde{x} & (\tilde{x} < 0) \\ \tilde{T}_b - \frac{Da_{III}\tilde{Y}_{R,f}}{\alpha_2^2 - \alpha_2}\exp(\alpha_2\tilde{x}) & (\tilde{x} > 0) \end{cases} \quad (46)$$

where β_1, β_2, C_3, and C_4 are constants:

$$\beta_1 = -\frac{Da_{III}C_1}{\alpha_1^2 - \alpha_1}$$
$$\beta_2 = -\frac{Da_{III}C_2}{\alpha_2^2 - \alpha_2}$$
$$C_3 = \frac{\left(\tilde{T}_f - \tilde{T}_s\right) - \left[1 - \exp\left(-\alpha_1\tilde{L}\right)\right]\beta_1 - \left[1 - \exp\left(-\alpha_2\tilde{L}\right)\right]\beta_2 - \tilde{r}_{pf}\tilde{L}}{1 - \exp\left(-\tilde{L}\right)}$$
$$C_4 = \tilde{T}_f - \beta_1 - \beta_2 - C_3 \quad (47)$$

For the solutions to satisfy the mass and heat flux continuity conditions (i.e., Eq. (23)), two additional relationships were obtained:

$$C_3 + \alpha_1\beta_1 + \alpha_2\beta_2 + \tilde{r}_{pf} = \left(\tilde{T}_f - \tilde{T}_b\right)\alpha_2 \quad (48)$$

$$\tilde{Y}_{R,f} = \frac{\left(\tilde{T}_b - \tilde{T}_f\right)\left(\alpha_2^2 - \alpha_2\right)}{Da_{III}} \quad (49)$$

Therefore, the Damkohler number and flame propagation speed could be numerically acquired.

Under the assumption (v), Eq. (49) can be further simplified as

$$\tilde{T}_f = \tilde{T}_b - \tilde{Y}_{R,f} \quad (50)$$

Under assumptions (v) and (vi), Eq. (48) can be transformed into

$$Da_{III} = \frac{1}{4}\left(\frac{\tilde{T}_b - \tilde{T}_s - \tilde{r}_{pf}\tilde{L}}{\tilde{T}_b - \tilde{T}_f}\right)^2 - \frac{1}{4} \quad (51)$$

which indicated that the flame was affected by the accumulation of pre-flame reactions occurring in the initial ($\tilde{T}_s$) and pre-flame ($\tilde{r}_{pf}\tilde{L}$) sections.

References

[1] Y. Liu, X. Sun, V. Sethi, D. Nalianda, Y. Li, L. Wang, Review of modern low emissions combustion technologies for aero gas turbine engines, Prog. Aerosp. Sci. 94 (2017) 12–45.
[2] F. Battin-Leclerc, Detailed chemical kinetic models for the low-temperature combustion of hydrocarbons with application to gasoline and diesel fuel surrogates, Prog. Energy Combust. Sci. 34 (4) (2008) 440–498.
[3] S. Zeppieri, L. Smith, M. Colket, Autoignition characteristics of selected alternative fuels at high OPR conditions, AIAA Propulsion and Energy Forum, AIAA, 2017 Paper 2017-4895.
[4] H. Mongia, TAPS: a fourth generation propulsion combustor technology for low emissions, AIAA International Air & Space Symposium & Exposition: The Next 100 Years, AIAA, 2003 Paper 2003-2657.
[5] C.K. Law, Combustion Physics, Cambridge University Press, Cambridge, UK, 2006.
[6] S.H. Won, B. Windom, B. Jiang, Y. Ju, The role of low temperature fuel chemistry on turbulent flame propagation, Combust. Flame 161 (2) (2014) 475–483.
[7] S.H. Won, S. Nakane, C.B. Reuter, B.C. Windom, Y. Ju, Effect of ignition chemistry on turbulent premixed flames of n-heptane and toluene, 53rd AIAA Aerospace Sciences Meeting, AIAA, 2015 Paper 2015-0430.
[8] B. Windom, S.H. Won, B. Jiang, Y. Ju, Detailed characterization of low temperature chemistry and turbulence interaction in reactor-assisted turbulent premixed flames, 52nd Aerospace Sciences Meeting, AIAA, 2014 Paper 2014-0313.
[9] B. Windom, S.H. Won, C.B. Reuter, B. Jiang, Y. Ju, S. Hammack, T. Ombrello, C. Carter, Study of ignition chemistry on turbulent premixed flames of n-heptane/air by using a reactor assisted turbulent slot burner, Combust. Flame 169 (2016) 19–29.
[10] A. Krisman, E.R. Hawkes, J.H. Chen, The structure and propagation of laminar flames under autoignitive conditions, Combust. Flame 188 (2018) 399–411.

[11] A. Krisman, C. Mounaïm-Rousselle, R. Sivaramakrishnan, J.A. Miller, J.H. Chen, Reference natural gas flames at nominally autoignitive engine-relevant conditions, Proc. Combust. Inst. 37 (2019) 1631–1638.
[12] C. Xu, J.W. Park, C.S. Yoo, J.H. Chen, T. Lu, Identification of premixed flame propagation modes using chemical explosive mode analysis, Proc. Combust. Inst. 37 (2019) 2407–2415.
[13] X. Gong, Z. Ren, Flame speed scaling in autoignition-assisted freely propagating n-heptane/air flames, Proc. Combust. Inst. (2021). https://doi.org/10.1016/j.proci.2020.07.029.
[14] J.B. Martz, H. Kwak, H.G. Im, G.A. Lavoie, D.N. Assanis, Combustion regime of a reacting front propagating into an auto-igniting mixture, Proc. Combust. Inst. 33 (2011) 3001–3006.
[15] O. Schulz, N. Noiray, Autoignition flame dynamics in sequential combustors, Combust. Flame 192 (2018) 86–100.
[16] O. Schulz, N. Noiray, Combustion regimes in sequential combustors: flame propagation and autoignition at elevated temperature and pressure, Combust. Flame 205 (2019) 253–268.
[17] O. Schulz, U. Doll, D. Ebi, J. Droujko, C. Bourquard, N. Noiray, Thermoacoustic instability in a sequential combustor: large eddy simulation and experiments, Proc. Combust. Inst. 37 (2019) 5325–5332.
[18] U.Doll D.Ebi, O. Schulz, Y. Xiong, N. Noiray, Ignition of a sequential combustor: evidence of flame propagation in the autoignitable mixture, Proc. Combust. Inst. 37 (2019) 5013–5020.
[19] T.C. Lieuwen, U.K. Cambridge, Unsteady Combustor Physics, Cambridge University Press, 2013.
[20] Y. Ju, B. Xu, Studies of the effects of radical quenching and flame stretch on mesoscale combustion, 44th AIAA Aerospace Sciences Meeting and Exhibit, AIAA, 2006 Paper 2006-1351.
[21] T. Zhang, Y. Ju, Structures and propagation speeds of autoignition-assisted premixed n-heptane/air cool and warm flames at elevated temperatures and pressures, Combust. Flame 211 (2020) 8–17.
[22] J.W. Dold, Premixed flames modelled with thermally sensitive intermediate branching kinetics, Combust. Theory Model. 11 (2007) 909–948.
[23] G.J. Sharpe, Effect of thermal expansion on the linear stability of planar premixed flames for a simple chain-branching model: the high activation energy asymptotic limit, Combust. Theory Model. 12 (2008) 717–738.
[24] L. Crocco, Research on combustion instability in liquid propellant rockets, Symp. (Int.) Combust. 12 (1969) 85–99.
[25] F.P. Mechel (Ed.), Formulas of acoustics, Springer-Verlag, Berlin Heidelberg, Germany, 2008.
[26] R.H. Natelson, M.S. Kurman, R.O. Johnson, N.P. Cernansky, D.L. Miller, Preignition and autoignition chemistry of the xylene isomers, Combust. Sci. Technol. 183 (2011) 897–914.
[27] Y. Pei, M. Mehl, W. Liu, T. Lu, W.J. Pitz, S. Som, A multicomponent blend as a diesel fuel surrogate for compression ignition engine applications, J. Eng. Gas Turbines Power 137 (11) (2015) 111502.
[28] Y. Morinishi, T.S. Lund, O.V. Vasilyev, P. Moin, Fully conservative higher order finite difference schemes for incompressible flow, J. Comput. Phys. 143 (1998) 90–124.
[29] S. Gottlieb, C.W. Shu, Total variation diminishing Runge–Kutta schemes, Math. Comput. 67 (1998) 73–85.
[30] J.A. van Oijen, Flamelet-Generated Manifolds: Development and Application to Premixed Laminar Flames, Technische Universiteit Eindhoven, Eindhoven, 2002.
[31] S. Deng, P. Zhao, M.E. Mueller, C.K. Law, Autoignition-affected stabilization of laminar nonpremixed DME/air coflow flames, Combust. Flame 162 (2015) 3437–3445.
[32] A. Vié, B. Franzelli, Y. Gao, T. Lu, H. Wang, M. Ihme, Analysis of segregation and bifurcation in turbulent spray flames: a 3D counterflow configuration, Proc. Combust. Inst. 35 (2015) 1675–1683.
[33] J.E. Temme, P.M. Allison, J.F. Driscoll, Combustion instability of a lean premixed prevaporized gas turbine combustor studied using phase-averaged PIV, Combust. Flame 161 (2014) 958–970.
[34] C.K. Westbrook, F.L. Dryer, Chemical kinetic modeling of hydrocarbon combustion, Prog. Energy Combust. Sci. 10 (1984) 1–57.
[35] G.P. Smith, D.M. Golden, M. Frenklach, N.M. Moriarty, B. Eiteneer, M. Goldenberg, C.T. Bowman, R.K. Hanson, S. Song, W.C. Gardiner Jr, V.V. Lissianski, GRI 3.0 Mechanism, Gas Research Institute, 1999. http://www.me.berkeley.edu/gri_mech.
[36] Z. Zhao, M. Chaos, A. Kazakov, F.L. Dryer, Thermal decomposition reaction and a comprehensive kinetic model of dimethyl ether, Int. J. Chem. Kinetics 40 (2008) 1–18.